Nanoscale oxygen defect gradients in UO_{2+x} surfaces

Steven R. Spurgeon[a,1], Michel Sassi[b], Colin Ophus[c], Joanne E. Stubbs[d], Eugene S. Ilton[b], and Edgar C. Buck[a]

[a]Energy and Environment Directorate, Pacific Northwest National Laboratory, Richland, WA 99352; [b]Physical and Computational Sciences Directorate, Pacific Northwest National Laboratory, Richland, WA 99352; [c]National Center for Electron Microscopy, Molecular Foundry, Lawrence Berkeley National Laboratory, Berkeley, CA 94720; and [d]Center for Advanced Radiation Sources, The University of Chicago, Chicago, IL 60439

Edited by David L. Clark, Los Alamos National Laboratory, Los Alamos, NM, and accepted by Editorial Board Member Richard Eisenberg July 15, 2019 (received for review March 25, 2019)

Oxygen defects govern the behavior of a range of materials spanning catalysis, quantum computing, and nuclear energy. Understanding and controlling these defects is particularly important for the safe use, storage, and disposal of actinide oxides in the nuclear fuel cycle, since their oxidation state influences fuel lifetimes, stability, and the contamination of groundwater. However, poorly understood nanoscale fluctuations in these systems can lead to significant deviations from bulk oxidation behavior. Here we describe the use of aberration-corrected scanning transmission electron microscopy and electron energy loss spectroscopy to resolve changes in the local oxygen defect environment in UO_{2+x} surfaces. We observe large image contrast and spectral changes that reflect the presence of sizable gradients in interstitial oxygen content at the nanoscale, which we quantify through first-principles calculations and image simulations. These findings reveal an unprecedented level of excess oxygen incorporated in a complex near-surface spatial distribution, offering additional insight into defect formation pathways and kinetics during UO_2 surface oxidation.

actinide oxides | uraninite | surface oxidation | scanning transmission electron microscopy | electron energy loss spectroscopy

The engineering of oxygen defects is a central focus of modern materials science. These defects influence the electronic, magnetic, optical, and radiation-response properties of materials in ways that are difficult to control and predict a priori (1–3). In particular, the safe use and disposal of oxide-based nuclear fuels depend on comprehensive models for oxidative processes and defect formation, which can guide operation, long-term waste storage, and accident cleanup efforts (4). Because of their strategic importance and potential environmental impact (5), the oxidative behavior of the actinides has attracted considerable attention. These $5f$ elements exist in multiple valence states in oxides, leading to electronic properties and phase transitions that are a sensitive function of oxygen defects.

Among the actinides, hyperstoichiometric UO_{2+x} has been examined for over half a century because of its central role in fuel production, as well as its many interesting properties (6–10). The system can adopt at least 14 known fluorite-derivative crystal structures, with oxidation states spanning $U^{4+} \rightarrow U^{6+}$, the latter of which is aqueous soluble and a risk driver for environmental transport (7, 8, 11). The complex chemical landscape of this system has motivated longstanding questions about the nature of these phase transitions and the incorporation of excess oxygen. Prior work indicated that a stoichiometry of $UO_{2.25}$ is readily attainable while preserving the nominal fluorite structure (12). However, several studies have identified metastable higher oxides possessing a fluorite-like structure, including U_3O_7 (13, 14) and U_3O_8 (15). The former studies found that the U sublattice is very similar between UO_2 and higher oxides up to U_3O_8 and that the main differences arise in the O anion sublattice. The latter study showed that it is possible to stabilize fluorite-like U_3O_8 at high temperature and pressure, which is retained upon quenching to ambient conditions. This experimental work is further supported by theory calculations (16, 17), which indicate that stoichiometries up to $UO_{2.5}$ should be possible within the fluorite-like structure. Together, these studies suggest that the primary impact of excess oxygen will be on the type and distribution of O anion defects, rather than a sizable distortion of the U cation sublattice. It is clear that nanoscale deviations from predicted bulk behavior, as well as nonequilibrium synthesis pathways, can greatly affect the oxidation process, calling for a more precise local understanding between phase transitions and oxygen defect formation.

While a large body of experimental and computational work has attempted to elucidate defect formation kinetics and oxidation pathways of UO_2, the task is hindered by a lack of well-controlled model systems and the difficulty of simulating strongly correlated $5f$ electrons (6, 8, 18). Most studies have relied on volume-averaged techniques, such as X-ray absorption near-edge structure (XANES), extended X-ray absorption fine structure (EXAFS), and X-ray photoelectron spectroscopy (XPS), applied to polycrystalline samples (19–22). When these measurements are interpreted through first-principles calculations, they can yield powerful insight into electronic structure, local coordination environment, and valence (21, 23, 24). In addition, X-ray crystal truncation rod (CTR) analysis has been shown to resolve surface distortions and subsurface oxygen interstitial profiles in single-crystal UO_2, albeit over a millimeter-sized region of a sample (25, 26). Through fitting the CTR data and computational modeling, the authors inferred the development of oscillatory interstitial O profiles under the (001)- and (111)-oriented surfaces of UO_2. However, the large atomic number contrast between U and O, as well as the large lateral area

Significance

Our study has far-reaching implications for the safe use of nuclear materials around the world. The strong oxidative tendency of the actinides drives contamination of groundwater near waste storage sites. A key finding of our study is that excess oxygen from the environment can be incorporated at far greater levels than previously thought, while still preserving the nominal cubic crystal structure of the widely used nuclear fuel UO_2. This insight, enabled by atomic-resolution spectroscopy and theory calculations, will allow us to develop better, more reliable models for nuclear waste storage and disposal.

Author contributions: S.R.S., M.S., C.O., J.E.S., E.S.I., and E.C.B. designed research; S.R.S., M.S., and C.O. performed research; C.O. contributed new reagents/analytic tools; S.R.S., M.S., C.O., J.E.S., E.S.I., and E.C.B. analyzed data; and S.R.S., M.S., C.O., J.E.S., E.S.I., and E.C.B. wrote the paper.

The authors declare no conflict of interest.

This article is a PNAS Direct Submission. D.L.C. is a guest editor invited by the Editorial Board.

Data deposition: Data from this study have been deposited in Figshare, https://figshare.com/articles/Spurgeon_UO2_PNAS_Data_Archive/9108503/1.

[1]To whom correspondence may be addressed. Email: steven.spurgeon@pnnl.gov.

This article contains supporting information online at www.pnas.org/lookup/suppl/doi:10.1073/pnas.1905056116/-/DCSupplemental.

Published online August 9, 2019.

over which the measurements were averaged, precluded the direct observation of interstitial geometries and localized atomic environments.

A major strength of scanning transmission electron microscopy and electron energy loss spectroscopy (STEM-EELS) approaches is that they provide high-resolution, simultaneous information about local structure, chemistry, and defects. Past studies have shown that STEM-EELS is capable of detecting minor changes in oxidation state and composition and that it compares favorably to X-ray results on similar uranium compounds (27–30). Within the dipole approximation, these results can also be modeled using first-principles methods, offering a means to quantify defect configurations and density (27, 31). However, early STEM-EELS work on the actinides was performed using slower, lower-resolution spectrometers (32–37) and few studies (38, 39) have leveraged the advanced instrumentation or the supporting first-principles computing power developed in recent years. Modern aberration-corrected microscopes, equipped with bright, subangstrom electron probes and high-speed EELS spectrometers, now permit true atomic-scale spectroscopy with exceptional energy resolution (40). Studies of complex oxides have shown that it is possible to examine image contrast (41) and spectral changes (42, 43) associated with oxygen defects at interfaces and around local inhomogeneities that lead to significant deviations from bulk properties, but are difficult to access via other means. These as-yet untapped techniques may inform atomistic mechanisms for uranium oxidation.

Here we compare the behavior of model oxidized (001)- and unoxidized (111)-oriented single-crystal UO_2 surfaces using a combination of aberration-corrected STEM imaging and spectroscopy supported by first-principles theory and image simulations. Data pertaining to this study have been deposited in Figshare ("Spurgeon UO2 PNAS Data Archive," https://figshare.com/articles/Spurgeon_UO2_PNAS_Data_Archive/9108503/1) (44). Previous X-ray CTR results (25, 26) have indicated that the former surface exhibits a 2-layer periodicity in surface-normal lattice contraction, which was indirectly related to the insertion of O interstitials. We present an atomically resolved STEM-EELS mapping of the U $M_{4,5}$ edge, as well as a detailed examination of the O K edge fine structure in the vicinity of the crystal surface. This combination of techniques provides unique insight into the basis for image contrast and the emergence of key spectral features that result from the incorporation of excess oxygen in the near-surface region. We quantify the local interstitial content at the nanoscale, finding a large amount of excess oxygen distributed across a gradient near the sample surface; however, we see no evidence for a large-scale phase transition from the fluorite structure even at stoichiometries approaching $UO_{\sim 2.67}$. Finally, we identify how these gradients impact the prior understanding of UO_2 oxidation and discuss how they might also inform the analysis of other actinides. Our results illustrate how direct, real-space imaging approaches can inform our understanding of oxygen defect formation in actinide oxides.

As described in *SI Appendix*, we prepared 2 model UO_2 single-crystal surfaces: An unoxidized (111)-oriented control sample stored in an inert gas environment and a heavily oxidized (001) sample exposed to pure O_2 for 21 d, followed by storage in ambient conditions for several months. The former has been predicted to be the most stable UO_2 surface when dry (25). We examined the cross-sectional structure of the near-surface region for each sample at atomic resolution, as shown in Fig. 1. These images were acquired in the incoherent STEM high-angle annular dark field (STEM-HAADF) imaging mode, whose contrast is approximately proportional to atomic number $Z^{\sim 1.7}$; this mode is insensitive to the thickness-dependent contrast reversals that complicate the interpretation of typical high-resolution transmission electron micrographs (45). Both samples, shown in Fig. 1 *A* and *B*, exhibited a single-crystalline structure free of extended defects or impurities and we confirmed a nominal cubic fluorite structure throughout, as described in *SI Appendix*. However, there is a striking difference in the contrast of the (001) crystal surface, which exhibited an $\sim$15-nm band of increased intensity. This band was present in all of the oxidized samples prepared and was not the result of carbon contamination or thickness variation, as confirmed by imaging and low-loss EELS shown in *SI Appendix*, Figs. S1 and S2. We also performed geometric phase analysis (GPA) to assess possible strain variations at the nanoscale, as shown in *SI Appendix*, Fig. S3. These results suggest that no large-scale phase transformation has occurred at the sample surface and that lattice bending is not responsible for the contrast band.

Interestingly, a study of CeO_2 nanoparticles (41) found that changes in ionic radius upon oxidation from $Ce^{3+} \rightarrow Ce^{4+}$ can impart static lattice displacements to the crystal; this, in turn, can influence electron channeling and induce sizable changes in

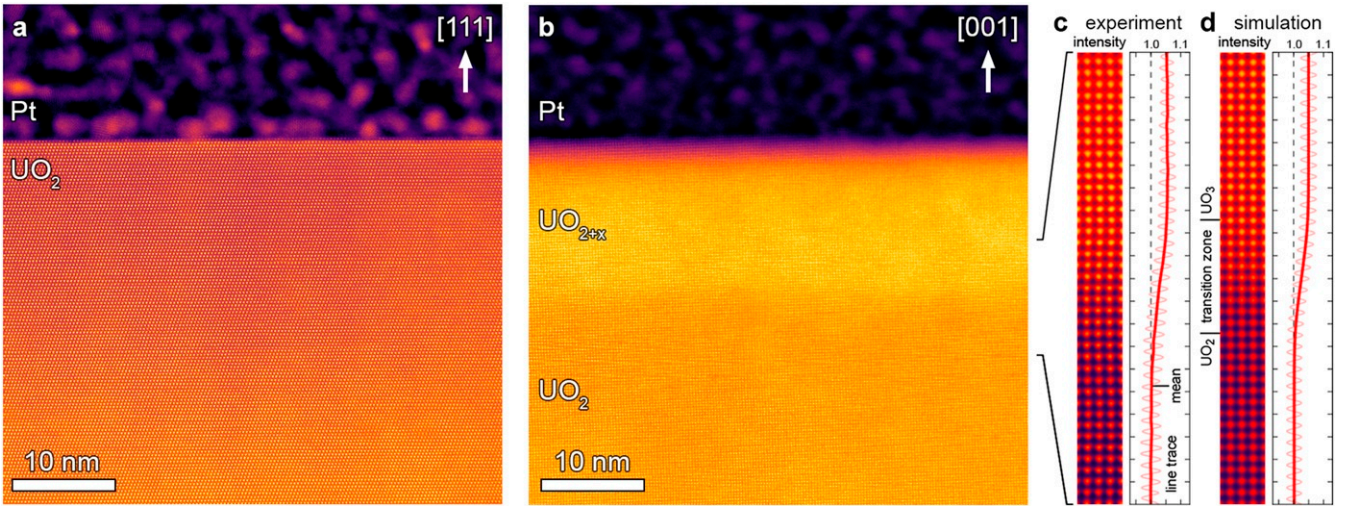

Fig. 1. Imaging and simulation of the UO_2 sample surfaces. (*A* and *B*) Colorized cross-sectional STEM-HAADF images of the unoxidized (111)-oriented (*A*) and oxidized (001)-oriented (*B*) UO_2 sample surfaces, respectively. These images are taken along the [110] and [100] zone axes, respectively. (*C* and *D*) Experimental (*C*) and simulated (*D*) mean unit cells, and corresponding line traces, for the (001) sample.

STEM image contrast. A simple estimate using Shannon ionic radii (46) shows that a transition from 8-fold–coordinated U^{4+} (1 Å) → 7-fold–coordinated U^{5+} (0.84 Å) → 8-fold–coordinated U^{6+} (0.86 Å) amounts to a 14% ion size reduction, in line with the change from Ce^{3+} (1.14 Å) → Ce^{4+} (0.97 Å) of 17.5%. While CeO_2 possesses a fluorite structure very similar to UO_2 and is often used as a proxy to simulate radiation damage effects (47), we expect even greater channeling behavior due to the higher atomic scattering factor of U ($Z = 92$) vs. Ce ($Z = 58$) (48). As shown in *SI Appendix*, Fig. S4, we performed an array of multislice image simulations for different UO_{2+x} chemistries to explore the effect of the configuration and density of oxygen defects on the resulting STEM-HAADF image contrast. Fig. 1*C* shows an experimental mean unit cell taken from Fig. 1*B*, highlighting the intense contrast of the near-surface region. This experimental cell is compared to a simulation where the stoichiometry is varied from UO_2 to UO_3 over 10 lattice planes in Fig. 1 *C* and *D*. The simulated image intensity shows good qualitative agreement with the experimental contrast gradient of 3% to 5%. A precise amount of excess interstitial oxygen cannot be determined from this comparison due to the relatively large sample thickness (55 to 60 nm) and computational limitations. However, our simulations combined with low-loss EELS thickness measurements (*SI Appendix*, Fig. S2) indicate that the most likely explanation for the higher intensity near the surface is a large amount of interstitial oxygen, which is consistent with prior CTR analysis (25, 26). These findings strongly suggest that the contrast gradient arises from changes in the local electron channeling, pointing to underlying changes in defect environment that can be probed spectroscopically.

Accordingly, we performed atomic-scale STEM-EELS mapping of the U $M_{4,5}$ and O K ionization edges for the 2 cross-sectional samples, as shown in Fig. 2. The U $M_{4,5}$ edge results from white-line transitions from the U $3d \rightarrow 5f$ states (39); its higher ionization energy compared to the $N_{4,5}$ ($4d \rightarrow 5f$) and $O_{4,5}$ ($5d \rightarrow 5f$) edges makes it an excellent candidate for localized composition mapping. The O K edge results from transitions from the O $1s \rightarrow$ O $2p$ – U $6d$ and O $1s \rightarrow$ O $2p$ – U $5f$ states, where U $5f$ and $6d$ hybridize with O $2p$ (23, 24); while more complex, this edge encodes detailed information about the U coordination environment and therefore offers a window into defects formed during oxidation. Although previous studies have examined trends in the U $M_{4,5}$ white-line ratio in EELS (34, 49), hardware limitations made it difficult to perform atomic-resolution mapping needed to understand local fluctuations in composition and chemistry at surfaces and interfaces. With the development of modern aberration correctors, the large probe convergence angles, high currents, and small probe sizes needed for atomic-scale spectroscopy are now available.

We focused our spectroscopic mapping on the problem of identifying signatures of interstitial oxygen defects, which required supporting first-principles calculations. Fig. 2*A* shows a composition map of the U $M_{4,5}$ edge collected at the unoxidized (111) surface, illustrating the excellent compositional uniformity and crystallinity of the sample up to its top monolayer. Fig. 2 *B* and *C* shows O K edge spectra extracted from a map of the (111) surface region, progressing from the topmost layer of the crystal to its bulk. The edge displays 2 sharp peaks at 533 and 538.75 eV, followed by a shoulder at 543.25 eV and 2 broader features at 553 and 566 eV. We note that the overall line shape is in good agreement with prior work (31) and that there is little variation upon moving from the surface (spectrum 1) to the bulk (spectrum 7).

In comparison, O K edge measurements of the oxidized (001) surface, shown in Fig. 2 *D* and *E*, exhibit markedly different behavior. The overall bulk spectrum 7 is quite similar to the (111) sample, with a minor change in the ratio of the 2 sharp peaks at lower energy loss. However, moving closer to the sample surface, there is a striking redistribution of spectral features that coincides with the presence of the surface contrast band (spectra 1 to 4). These features are highlighted in the difference spectra in Fig. 2 *F* and *G*. Notably, we observe the emergence of a distinct shoulder at 530.5 eV (feature 1), changes in the ratio of the 2 main peaks (features 2 and 4), and an increase in the minimum at 535.5 eV (feature 3), as well as the emergence of a broad peak at 548 eV (feature 5). Collectively these results suggest the possibility of distinct local structures giving rise to these spectral features in the oxidized (001) surface.

We therefore turned to first-principles theory calculations using the density functional theory (DFT) framework to explore possible defect structures that could give rise to the measured spectral features. Within the dipole approximation (valid at our primary beam energy of 200 to 300 kV), calculated XANES spectra can be compared to measured EELS spectra, since they probe the same electronic states; these comparisons provide valuable insight and are commonly used to rationalize observed trends and fine structure features in oxides. While a ground-state approach cannot account for excited core-hole effects, they have been shown to have little influence on the predicted energy-loss

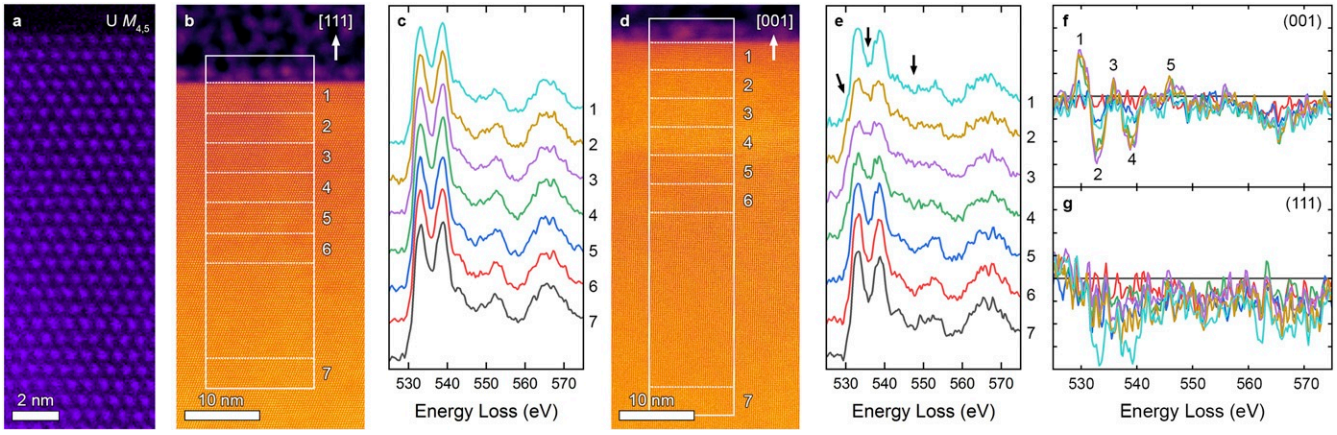

Fig. 2. Spectroscopy of the UO_2 sample surfaces. (*A*) STEM-EELS composition map of the U $M_{4,5}$ edge measured at the unoxidized (111) sample surface. (*B* and *C*) STEM-HAADF image of the (111) surface and corresponding O *K* edge spectra extracted from the numbered windows, respectively. (*D* and *E*) STEM-HAADF image of the oxidized (001) surface and corresponding O *K* edge spectra extracted from the numbered windows, respectively. (*F* and *G*) Difference plots showing changes in spectral features relative to the bulk, marked by 1 to 5, for the (001)- and (111)-oriented sample surfaces, respectively.

near-edge structure (ELNES) in the fluorites (50). Using the FDMNES code (51), we calculated O K edge XANES spectra for both pristine and defective UO_2 containing either an oxygen interstitial or a vacancy (*SI Appendix*).

The calculated spectrum for bulk defect-free UO_2 is in good agreement with experimental measurements deep in the bulk of the sample; as shown in *SI Appendix*, Fig. S6, all of the spectral features and relative intensity of the 2 sharp experimental peaks at 533 and 538.75 eV are well reproduced. An analysis of the density of states reveals that these 2 first peaks can be assigned to O $1s$ to O $2p$ – U $5f$ and O $2p$ – U $6d$ transitions, in good agreement with previous work which also noted the significant hybridization between the O $2p$ and U $5f$ and $6d$ orbitals (19–21). While previous work (19) has determined that the EXAFS features in UF_4, a compound sharing some similarities with UO_2, affect the K edge from 30 eV beyond the beginning of the edge, we do not expect that EXAFS features will significantly affect the first 2 first peaks of the O K edge because they span an energy range only up to 15 eV beyond the beginning of the edge.

The introduction of an interstitial O in the lattice deforms the surrounding environment, breaking the high cubic symmetry of UO_2 and breaking degeneracies in U–O bonding. Accordingly, 2 component spectra were calculated: One is the average of all of the lattice site O atoms, and the other is for the interstitial O atom, shown by the blue and orange curves in Fig. 3, respectively. These 2 component spectra show differences compared to the one calculated for a defect-free high cubic symmetry UO_2 (*SI Appendix*, Fig. S7); in particular, for the lattice O sites we find that the relative intensity of the 2 first peaks, labeled 1 and 2 in Fig. 3*A*, is reversed, with peak 2 being less intense than peak 1. Especially interesting is the calculated spectrum for the interstitial O atom in UO_2, which exhibits completely different spectral features compared to the one from lattice O sites. Three features—labeled *a*, *b*, and *c*—emerge that correspond to the positions of the experimentally observed changes indicated by arrows in Fig. 2*E*. These features are positioned such that the 2 minima of the interstitial O spectra, located between *a* and *b*, and *b* and *c*, overlap with peaks 1 and 2 of the lattice O site spectra, while the peak *b* is aligned with the minimum in between peaks 1 and 2. The contributions of lattice and interstitial O are shown for clarity in Fig. 3*C*. Another interesting characteristic in the spectra of interstitial O is that the minimum between *b* and *c* has a higher intensity than the minimum between *a* and *b*. Therefore, performing a linear combination of the calculated lattice and interstitial O K edge component spectra leads to an increase of the intensity of peak 2 greater than that of peak 1 and fills the minimum between those peaks, as seen by the green linear combination fit curves shown in Fig. 3.

To compare and qualitatively reproduce the changes observed in the oxidized (001) sample, we varied the contribution of the O interstitial component in the linear combination and varied the broadening of the calculated spectra to best match the experimental one for each case. As shown in Fig. 3 *A* and *B*, the best fit—considering the relative intensity between peaks 1 and 2, as well as the minimum in between—yields a much larger amount of interstitials for the near surface (spectrum 3) than for the bulk (spectrum 7). The fits suggest that the stoichiometry of the material in the region of spectrum 3 is closer to $UO_{2.6667}$, while it is less than $UO_{2.0833}$ for the bulk region of spectrum 7 (nominally UO_2), as shown in Fig. 3*D*. Recognizing that the overall trend is certainly more reliable than absolute compositional values, it is nonetheless clear that there is a gradient in the interstitial distribution in the (001) sample and that the region near spectrum 3 contains significantly more interstitial O atoms compared to the bulk region.

These findings are consistent with our imaging and multislice simulations, which show that a sizable interstitial O content is needed to reproduce the experimental contrast. While a combination of other defects may be involved in the change of spectral features, we note that neither O vacancies nor a homogeneous lattice expansion or contraction can effectively reproduce the spectral changes. As shown in *SI Appendix*, Fig. S7, the filling of the minimum in between peaks 1 and 2, as well as the overall intensity increase of the postpeak 2 shoulder, cannot be reproduced in these scenarios. Rather, we find that the unique spectral features observed in the sample can best be described by interstitial oxygen defects that affect the U coordination environment.

In summary, we observe an unprecedented large amount of interstitial oxygen distributed across a nanoscale gradient in the (001) surface. Importantly, we find no evidence for large-scale phase transformations, suggesting that a stoichiometry of nearly $UO_{2.67}$ is attained in the fluorite structure; this value is

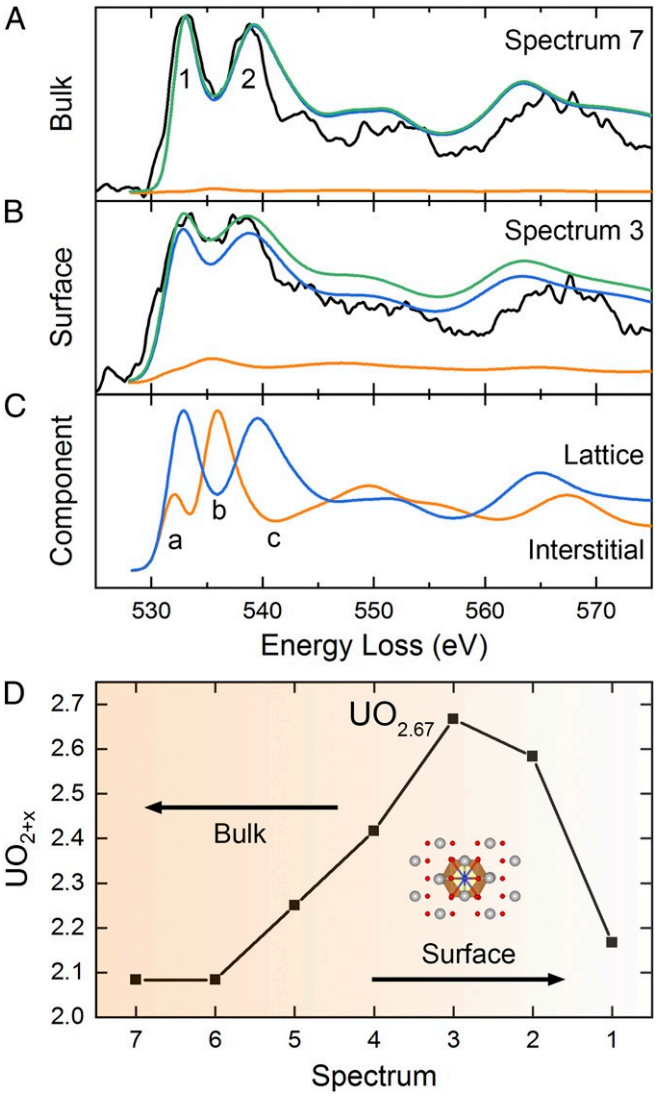

Fig. 3. Analysis of oxygen defect environment in the (001) sample. (*A* and *B*) Comparison between experimental EELS and theoretically calculated XANES spectra accounting for the presence of interstitial oxygen for the bulk spectrum 7 (*A*) and near-surface spectrum 3 (*B*), respectively. The experimental data (black), contributions from O lattice sites (blue), interstitial O (orange), and the resulting linear combinations (green) are shown. Key emergent features are marked by *a*–*c* in *C*. (*C*) Calculated O lattice site (blue) and interstitial O (orange) components, normalized to the same scale. (*D*) Estimate of effective local stoichiometry per unit cell. *Inset* shows an illustration of the oxygen defect formed.

comparable to the highest U_3O_8 stoichiometry obtained during high-pressure synthesis (15), and in excess of prior reports on the formation of U_3O_7 (13, 14), representing a significant departure from bulk behavior. Considering the nonequilibrium nature of the oxidative process, we emphasize the competition of the bulk and surface states of the crystal. Analogous to substrate-induced "clamping" in multiferroic oxide heterostructures (52), it is likely that structural distortions of the surface are constrained by the underlying bulk, limiting associated phase transitions. The competition between transport of oxygen into the bulk and reduction of the surface may also give rise to the observed gradient in oxygen interstitial content. These nanoscale insights can help refine our understanding of oxygen transport and defect formation kinetics in this system. More broadly, our study shows how a combination of STEM, EELS, and first-principles calculations may be used to fingerprint the local chemical environment of actinide surfaces. Substantial excess oxygen manifests in image contrast changes that are accompanied by unique spectral signatures in the O K edge fine structure. Our simulations are able to disentangle key contributors to these signatures, identifying likely oxygen configurations that can be examined in other related systems. Using this approach, it is now possible to examine defect generation at surfaces and interfaces, such as grain boundaries in altered spent nuclear fuel pellets or other actinide oxide waste forms, paving the way for more comprehensive atomistic models for oxidative behavior.

Additional Information

SI Appendix details the methods used, imaging, thickness measurements, strain analysis, multislice simulation, and first-principles calculations. Correspondence and requests for materials should be addressed to S.R.S.

ACKNOWLEDGMENTS. S.R.S. thanks Drs. Kevin Rosso, Demie Kepaptsoglou, and Lewys Jones for helpful discussions. Pacific Northwest National Laboratory (PNNL) is a multiprogram national laboratory operated for the Department of Energy (DOE) by Battelle. This work was supported by the Nuclear Process Science Initiative at PNNL. A portion of the microscopy was performed in the Radiological Microscopy Suite, located in the Radiochemical Processing Laboratory at PNNL. Work at the Molecular Foundry was supported by the Office of Science, Office of Basic Energy Sciences, of the US DOE under Contract DE-AC02-05CH11231. C.O. acknowledges support from the DOE Early Career Research Program. J.E.S. is supported by the National Science Foundation-Earth Sciences (EAR-1634415) and DOE-GeoSciences (DE-FG02-94ER14466 and DE-SC0019108). We thank R. Caciuffo (Institute for Transuranium Elements) and M. Paffett (Los Alamos National Laboratory) for providing the UO_2 crystals.

1. H. L. Tuller, S. R. Bishop, Point defects in oxides: Tailoring materials through defect engineering. *Annu. Rev. Mater. Res.* **41**, 369–398 (2011).
2. M. Verónica Ganduglia-Pirovano, A. Hofmann, J. Sauer, Oxygen vacancies in transition metal and rare earth oxides: Current state of understanding and remaining challenges. *Surf. Sci. Rep.* **62**, 219–270 (2007).
3. K. E. Sickafus *et al.*, Radiation tolerance of complex oxides. *Science* **289**, 748–751 (2000).
4. P. C. Burns, R. C. Ewing, A. Navrotsky, Nuclear fuel in a reactor accident. *Science* **335**, 1184–1188 (2012).
5. R. M. Coyte *et al.*, Large-scale uranium contamination of groundwater resources in India. *Environ. Sci. Technol. Lett.* **5**, 341–347 (2018).
6. M. W. D. Cooper, S. T. Murphy, D. A. Andersson, The defect chemistry of UO2±x from atomistic simulations. *J. Nucl. Mater.* **504**, 251–260 (2018).
7. D. W. Shoesmith, Fuel corrosion processes under waste disposal conditions. *J. Nucl. Mater.* **282**, 1–31 (2000).
8. R. J. McEachern, P. Taylor, A review of the oxidation of uranium dioxide at temperatures below 400°C. *J. Nucl. Mater.* **254**, 87–121 (1998).
9. E. S. Fisher, The first 30 years of research on the physical properties of α-U. *J. Alloys Compd.* **213-214**, 254–261 (1994).
10. B. Wasserstein, Ages of uraninites by a new method. *Nature* **174**, 1004–1005 (1954).
11. K. O. Kvashnina, S. M. Butorin, P. Martin, P. Glatzel, Chemical state of complex uranium oxides. *Phys. Rev. Lett.* **111**, 253002 (2013).
12. B. T. M. Willis, The defect structure of hyper-stoichiometric uranium dioxide. *Acta Crystallogr. Sect. A* **34**, 88–90 (1978).
13. L. Desgranges, G. Baldinozzi, G. Rousseau, J.-C. Niepce, G. Calvarin, Neutron diffraction study of the in situ oxidation of UO 2. *Inorg. Chem.* **48**, 7585–7592 (2009).
14. F. Garrido, R. M. Ibberson, L. Nowicki, B. T. M. Willis, Cuboctahedral oxygen clusters in U3O7. *J. Nucl. Mater.* **322**, 87–89 (2003).
15. F. X. Zhang *et al.*, High-pressure U3O8 with the fluorite-type structure. *J. Solid State Chem.* **213**, 110–115 (2014).
16. D. A. Andersson, G. Baldinozzi, L. Desgranges, D. R. Conradson, S. D. Conradson, Density functional theory calculations of UO 2 oxidation: Evolution of UO 2+ x, U 4 O 9– y, U 3 O 7, and U 3 O 8. *Inorg. Chem.* **52**, 2769–2778 (2013).
17. M. Molinari, N. A. Brincat, G. C. Allen, S. C. Parker, Structure and properties of some layered U 2 O 5 phases: A density functional theory study. *Inorg. Chem.* **56**, 4468–4473 (2017).
18. T. Vitova *et al.*, The role of the 5f valence orbitals of early actinides in chemical bonding. *Nat. Commun.* **8**, 1–9 (2017).
19. J. G. Tobin *et al.*, Covalency in oxidized uranium. *Phys. Rev. B* **92**, 045130 (2015).
20. D. L. Clark, *Chemical bonding in molecules with valence 5f-electrons*. https://www.osti.gov/servlets/purl/1119596. Accessed 1 June 2019.
21. S.-W. Yu *et al.*, f-f origin of the insulating state in uranium dioxide: X-ray absorption experiments and first-principles calculations. *Phys. Rev. B* **83**, 165102 (2011).
22. E. S. Ilton, P. S. Bagus, XPS determination of uranium oxidation states. *Surf. Interface Anal.* **43**, 1549–1560 (2011).
23. Z. Y. Wu *et al.*, X-ray absorption at the oxygen K edge in cubic f oxides examined using a full multiple-scattering approach. *J. Phys. Condens. Matter* **11**, 7185–7194 (1999).
24. F. Jollet *et al.*, The electronic structure of uranium dioxide: An oxygen K-edge x-ray absorption study. *J. Phys. Condens. Matter* **9**, 9393–9401 (1997).
25. J. E. Stubbs *et al.*, Oxidative corrosion of the UO2(001) surface by nonclassical diffusion. *Langmuir* **33**, 13189–13196 (2017).
26. J. E. Stubbs *et al.*, UO2 oxidative corrosion by nonclassical diffusion. *Phys. Rev. Lett.* **114**, 246103 (2015).
27. A. K. Jiang *et al.*, Determination of interstitial oxygen atom position in U2N3+xOy by near edge structure study. *J. Nucl. Mater.* **504**, 215–220 (2018).
28. J. G. Tobin, D. K. Shuh, Electron spectroscopy of the oxidation and aging of U and Pu. *J. Electron Spectros. Relat. Phenom.* **205**, 83–91 (2015).
29. R. Caciuffo, E. C. Buck, D. L. Clark, G. Van Der Laan. Spectroscopic characterization of actinide materials. *MRS Bull.* **35**, 889–895 (2010).
30. K. T. Moore *et al.*, Electron-energy-loss spectroscopy and X-ray absorption spectroscopy as complementary probes for complex f-electron metals: Cerium and plutonium. *Philos. Mag.* **84**, 1039–1056 (2004).
31. J. A. Aguiar, Q. M. Ramasse, M. Asta, N. D. Browning, Investigating the electronic structure of fluorite-structured oxide compounds: Comparison of experimental EELS with first principles calculations. *J. Phys. Condens. Matter* **24**, 295503 (2012).
32. S. Utsunomiya, M. Kogawa, E. Kamiishi, R. C. Ewing, "Scanning transmission electron microscopy and related techniques for research on actinide and radionuclide nanomaterials" in *Actinide Nanoparticle Research* (Springer Berlin Heidelberg, Berlin, Heidelberg, Germany, 2011), pp. 33–62.
33. E. C. Buck, M. Douglas, R. S. Wittman, Verifying the presence of low levels of neptunium in a uranium matrix with electron energy-loss spectroscopy. *Micron* **41**, 65–70 (2010).
34. M. Colella, G. R. Lumpkin, Z. Zhang, E. C. Buck, K. L. Smith, Determination of the uranium valence state in the brannerite structure using EELS, XPS, and EDX. *Phys. Chem. Miner.* **32**, 52–64 (2005).
35. S. L. Dudarev *et al.*, Understanding STM images and EELS spectra of oxides with strongly correlated electrons: A comparison of nickel and uranium oxides. *Micron* **31**, 363–372 (2000).
36. S. B. Rice, H. H. Bales, J. R. Roth, A. L. Whiteside, Empirical identification of uranium oxides and fluorides using electron energy-loss spectroscopy in the transmission electron microscope. *Microsc. Microanal.* **5**, 437–444 (1999).
37. H. Xu, Y. Wang, Electron energy-loss spectroscopy (EELS) study of oxidation states of Ce and U in pyrochlore and uraninite – natural analogues for Pu- and U-bearing waste forms. *J. Nucl. Mater.* **265**, 117–123 (1999).
38. A. Ochiai *et al.*, Uranium dioxides and debris fragments released to the environment with cesium-rich microparticles from the Fukushima Daiichi nuclear power plant. *Environ. Sci. Technol.* **52**, 2586–2594 (2018).
39. C. Degueldre, R. Schaeublin, J. Krbanjevic, E. Minikus, Electron energy loss spectroscopy investigation through a nano ablated uranium dioxide sample. *Talanta* **106**, 408–413 (2013).
40. O. L. Krivanek *et al.*, An electron microscope for the aberration-corrected era. *Ultramicroscopy* **108**, 179–195 (2008).
41. A. C. Johnston-Peck *et al.*, Oxidation-state sensitive imaging of cerium dioxide by atomic-resolution low-angle annular dark field scanning transmission electron microscopy. *Ultramicroscopy* **162**, 52–60 (2016).
42. J. A. Mundy, Q. Mao, C. M. Brooks, D. G. Schlom, D. A. Muller, Atomic-resolution chemical imaging of oxygen local bonding environments by electron energy loss spectroscopy. *Appl. Phys. Lett.* **101**, 042907 (2012).
43. M. Varela *et al.*, Atomic-resolution imaging of oxidation states in manganites. *Phys. Rev. B* **79**, 085117 (2009).
44. S. Spurgeon *et al.*, Data from "Spurgeon UO2 PNAS Data Archive." Figshare. 10.6084/m9.figshare.9108503.v1. Deposited 25 July 2019.
45. D. B. Williams, C. B. Carter, *Transmission Electron Microscopy* (Springer, 2009).
46. R. D. Shannon, Revised effective ionic radii and systematic studies of interatomic distances in halides and chalcogenides. *Acta Crystallogr. Sect. A* **32**, 751–767 (1976).

47. C. L. Tracy *et al.*, Redox response of actinide materials to highly ionizing radiation. *Nat. Commun.* **6**, 1–9 (2015).
48. L.-M. Peng, Electron atomic scattering factors and scattering potentials of crystals. *Micron* **30**, 625–648 (1999).
49. J. A. Fortner, E. C. Buck, A. J. G. Ellison, J. K. Bates, EELS analysis of redox in glasses for plutonium immobilization. *Ultramicroscopy* **67**, 77–81 (1997).
50. J. A. Aguiar *et al.*, Electronic structure of oxide fuels from experiment and first principles calculations., *J. Phys. Conf. Ser.* **241**, 012062 (2010).
51. O. Bunău, Y. Joly, Self-consistent aspects of x-ray absorption calculations. *J. Phys. Condens. Matter* **21**, 345501 (2009).
52. I. Bichurin, M. Petrov, G. Srinivasan, Theory of low-frequency magnetoelectric coupling in magnetostrictive-piezoelectric bilayers. *Phys. Rev. B Condens. Matter Mater. Phys.* **68**, 1–13 (2003).